



HAL
open science

Numerical investigation of the dynamical behavior of a fluid-filled microparticle suspended in human arteriole

Phd, Dr Imane El Jirari, Adil El Baroudi, Amine Ammar

► To cite this version:

Phd, Dr Imane El Jirari, Adil El Baroudi, Amine Ammar. Numerical investigation of the dynamical behavior of a fluid-filled microparticle suspended in human arteriole. *J Biomech Eng*, 2021, 10.1115/1.4049955 . hal-03951641

HAL Id: hal-03951641

<https://hal.science/hal-03951641>

Submitted on 23 Jan 2023

HAL is a multi-disciplinary open access archive for the deposit and dissemination of scientific research documents, whether they are published or not. The documents may come from teaching and research institutions in France or abroad, or from public or private research centers.

L'archive ouverte pluridisciplinaire **HAL**, est destinée au dépôt et à la diffusion de documents scientifiques de niveau recherche, publiés ou non, émanant des établissements d'enseignement et de recherche français ou étrangers, des laboratoires publics ou privés.

Numerical investigation of the dynamical behavior of a fluid-filled microparticle suspended in human arteriole

I. El Jirari

LAMPA, Arts et Metiers Institute
of Technology, HESAM University,
49035 Angers, France

A. El Baroudi

LAMPA, Arts et Metiers Institute
of Technology, HESAM University,
49035 Angers, France

A. Ammar

LAMPA, Arts et Metiers Institute
of Technology, HESAM University,
49035 Angers, France

ABSTRACT

*The study of artificial **microparticles** (capsules and vesicles) has gained a growing interest with the emergence of bioengineering. One of their promoting applications is their use as therapeutic vectors for drug delivery, when capsules and vesicles release their capacity in a targeted environment. The dynamic behavior of capsules and vesicles in confined or unbounded flows was widely studied in the literature and their mechanical response was truthfully described using constitutive laws with good agreement with experiences. However, in a context of biological application, to our knowledge, none of published studies investigating the mechanical response of deformable microparticle took into account the real physiological conditions: the rheological properties of blood such as carrying fluid and the mechanical properties of blood vessels. In this paper, we **consider** a hyperelastic microparticle suspended in human arteriole. We investigate the deformation of the microparticle resulting from its interaction with blood flow and the **arteriolar** wall using various capillary numbers and respecting physiological properties of blood and arterial wall. The influence of the blood viscosity model (Newtonian vs shear-thinning) is investigated and a comparison with a rigid microchannel **and a muscle-embedded arteriole** are carried out. The fluid structure interaction (FSI) problem is solved using Arbitrary Lagrangian Eulerian (ALE) method. **Our simulations have revealed that the arteriolar wall distensibility deeply influences both the deformation and velocity of the microparticle: the deformation strongly increases while the velocity decreases in comparison to an infinitely rigid wall. In the context of therapeutic procedure of targeted drug-delivery, a particular attention should be addressed to these observations, in particular for their implication in the burst mechanism.***

1 Introduction

Microencapsulation is the industrial process by which a droplet or a solid is enclosed by a thin elastic membrane, resulting in structures called microparticles. The membrane of a microparticle bursts under predetermined conditions allowing a controlled and targeted release of the inner contain. The application field of **microparticles** as delivery system includes cosmetics, pharmaceuticals and food. Microparticles are used as pharmaceutical vehicle in targeted drug delivery process for non-invasive cancer treatments [1–3], diabetes [4] and heart attack [5]. **In the procedure of targeted drug delivery, microparticles are injected into arterial bloodstream (e.g the hepatic artery for transarterial chemoembolization (TACE) [6] and the coronary arteries for thrombus dissolution [5]).** Once the microparticle is injected, it flows in varied size and nature blood vessels till it reaches its target (e.g. tumor), a robust and reliable prediction of the mechanical behavior of microparticle (velocity, surface

tensions acting on membrane, deformation, burst. . .) and fluid kinetics (diffusion, convection, concentration of the released inner drug) in interaction with vascular wall and blood stream are essential to ensure a proper, efficient and safe functioning of the targeted drug-delivery procedure. Attention also should be addressed on local perturbation due to the presence of the microparticle (i.e. wall shear stress, pattern of blood flow...). Prediction and evaluation of drug-eluting microparticle behavior are conducted by means of in-vitro [7–9] and in-vivo [10] studies. Above-mentioned studies are conducted by physicians and focused on the pharmacokinetic behavior of the released drug without any consideration of mechanics. Interestingly, the present study proposes an alternative in-silico approach that could be complementary of in-vivo and in-vitro studies, by providing an upstream prediction of the mechanical behavior of the microparticle in its interaction with blood flow and vascular wall without tricky experimental protocols and limitations imposed by regulation related to animal experimentation. Furthermore, microparticles constitute an efficient biomimetic system to understand the mechanical properties of biological microparticles such as the red blood cell (RBC). The study of mechanical properties of RBCs and their dynamical response to applied external flow has profited from the enhancement of microfluidic devices where microchannels mime the vascular system [11, 12]. RBC is a biological cell formed by an elastic membrane (phospholipid bilayer attached to a spectrine skeleton) enclosing hemoglobin solution. Due to its finite thickness, only the deformation of median surface is considered. RBC membrane is characterized by three elastic moduli: surface shear modulus $G_s = 2.5 \mu\text{N/m}$ [13], surface extension modulus $K = 300 - 500 \text{ mN/m}$ [14–16] and bending rigidity (also called bending energy) $B = 5 - 150 \text{ K}_b\text{T}$ [17, 18]. In the microcirculation, RBCs are highly deformed from their initial biconcave shape. Depending on the blood flow strength and inner diameter of microvessel, RBCs take the shape of a bullet, a parachute or a slipper [19–21]. These characteristic shapes are also observed for artificial microparticles like vesicles and capsules [22–25]. Vesicle membrane is lipidic and acts like a bidimensional incompressible fluid (i.e. zero shear elasticity). In contrast, polymeric membrane of capsule is solid and shear resistant. Capsule’s membrane obeys to Lagrangian elastic laws. Instead of a reference configuration, vesicle membrane is characterized by an initial curvature which means a bending resistance. Mechanical properties of microparticles are obtained by different methods among them squeezing microparticle between two parallel plates [25, 26], spinning capsule experiment [27] flowing in a capillary tube [24, 28], micropipette aspiration [29], and compression [30]. In literature, membrane is assumed to obey different hyperelastic constitutive laws that describe hyperelasticity in terms of a strain energy potential which defines the strain energy stored in the material per unit of reference volume: Skalak (SK) [31–33], Evans-Skalak (ES) [32], Mooney-Rivlin (MR) [34], Neo-Hookean (NH) [35–37] and Yeoh [26]. For small strains, all of aforementioned hyperelastic laws reduce to the elastic Hook’s law [38]. Skalak law was first introduced to model the large deformation and area incompressibility of biological membrane [39], this law adds non-linearly the area dilatation to the shear deformation. Evans law (or Evans-Skalak law) [40] was introduced later to simplify SK law by adding linearly the area dilatation to the shear deformation. Due to its 3D origin, MR is strain-softening. NH law is derived from MR and Yeoh law is a higher-order extension of the NH law [41]. SK law is strain-hardening, hence, for similar hydrodynamic constraints a membrane obeying SK law is less deformed than the one obeying MR law [33] or NH law [24]. Besides constitutive law, microparticle deformation depends on viscosities ratio [42], the section of the microfluidic channel [36], membrane thickness [43], confinement [22, 25] and bending rigidity [44, 45].

In his Phd thesis [46], Tahiri introduced a local elastic law to take into account the contribution of the wall, nonetheless, without any consideration of the mechanical properties of the arterial wall. In this paper, we chose not to distinguish between a capsule and a vesicle (even if capsules are sometimes used to designate both artificial particles). Henceforth, the generic term microparticle is used to describe a Newtonian and incompressible fluid enclosed by a thin hyperplastic membrane.

In this study and in a context of medical application, we respect mechanical properties of arteriolar wall and the rheological/dynamical properties of blood flow in a human arteriole. The study is carried out using Arbitrary Lagrangian Eulerian Method implemented on Comsol Multiphysics [47].

2 Physical model description and modeling

The studied problem is schematically represented by a thin membrane enclosing an internal fluid, freely suspended in a confined external flow (blood). The arteriole is represented using a rectangular channel on which we distinguish the lumen and the arteriolar wall (see Figure 1). The flow is defined using an inlet velocity (at Γ_i) and a zero outlet normal stress (at Γ_o). The top-bottom right and left edges of the arterial wall are fixed. Three fluid-structure interfaces are identified: external fluid-membrane/internal fluid-membrane (Γ_{fm}) and external fluid-arterial wall (Γ_{fa}).

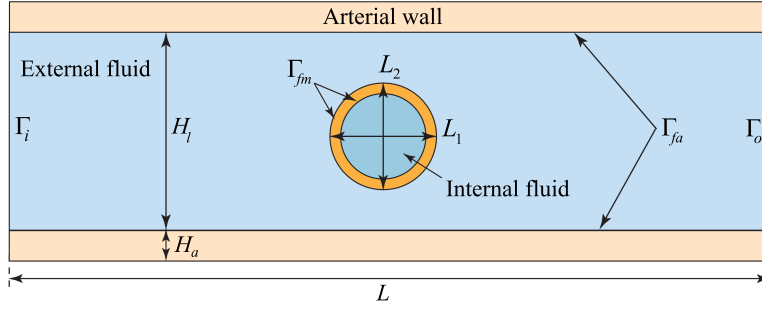


Fig. 1. Schematic description of the FSI problem.

2.1 Blood model

Blood is known to behave like a shear-thinning fluid in regions when shear rate $\dot{\gamma}$ is below 100s^{-1} [48–50], above this value, blood viscosity tend to a constant Newtonian viscosity $\eta = 0.0035\text{Pa}\cdot\text{s}$. In an arteriole, the shear rate exceeds significantly 100s^{-1} [51, 52] and blood is Newtonian. Even if non-Newtonian blood in the arteriole is physiologically implausible, we studied besides the Newtonian blood a specific case where blood is shear-thinning, the aim being to evaluate the effect of blood viscosity model on microparticle deformation. A Carreau model is used to describe the shear thinning of blood:

$$\eta = \eta_{\infty} + (\eta_0 - \eta_{\infty}) \left[1 + (\lambda\dot{\gamma})^2 \right]^{\frac{n-1}{2}} \quad (1)$$

where the coefficients $\eta_{\infty} = 0.0035\text{Pa}\cdot\text{s}$, $\eta_0 = 0.056\text{Pa}\cdot\text{s}$, $\lambda = 3.313\text{s}$ and $n = 0.3568$ were provided from [53]. Due to cardiac contractions, blood flow is pulsed, mainly in the arterial circulation. The disintisibility of arterial wall damps the pulsation of blood and transform the pulsatile flow into a continued flow (Windkessel effect). In biofluid mechanics, the importance of cyclic behavior in a pulsatile flow is quantified by Womersley number (α) [54]. This nondimensional number can be interpreted as the ratio of the unsteady forces to the viscous forces. Blood velocity profile depends on the Womersley number: for small and medium-sized arteries ($1 < \alpha < 10$) [55], flow is dominated by viscous effects and the profile is parabolic. For $\alpha > 10$, the unsteadiness dominates the flow, hence, velocity profile becomes blunted [56]. In the arteriole the Womersley number is approximately $\alpha = 0.016$, then we considered a steady Poiseuille flow described as:

$$v_i = 6v_0 \frac{y}{H_l} \left(1 - \frac{y}{H_l} \right) \quad \text{at } (\Gamma_i) \quad (2)$$

where $v_0 = 10\text{cm/s}$ is the average velocity in the arteriole and $H_l = 30\mu\text{m}$ the height of the rigid channel/arteriole. The value of H_l corresponds to the inner diameter (lumen) of a human arteriole and the corresponding arterial wall thickness is $H_a = 20\mu\text{m}$ [57]. In the absence of body forces, the incompressible flow is governed by the Navier-Stokes and continuity equations as given below

$$\begin{aligned} \rho \left[\frac{\partial \mathbf{v}}{\partial t} + (\mathbf{v} \cdot \nabla) \mathbf{v} \right] &= \nabla \cdot \boldsymbol{\sigma} \\ \nabla \cdot \mathbf{v} &= 0 \end{aligned}$$

where $\rho = 1050\text{kg/m}^3$ is the fluid density, \mathbf{v} is the velocity field, $\boldsymbol{\sigma}$ is the total stress in the incompressible fluid which could be expressed as :

$$\boldsymbol{\sigma} = -p\mathbf{I} + \eta \left[\nabla \mathbf{v} + (\nabla \mathbf{v})^T \right]$$

where p is the fluid pressure, \mathbf{I} is the identity tensor and η is the fluid dynamic viscosity.

2.2 Arterial wall model

The arterial wall consists of collagen, elastin and smooth muscle cells distributed and oriented differently on three distinct layers: the intima, the media and the adventice [58]. Layer-specific mechanical properties of human coronary artery include nonlinearity, inelasticity and anisotropy [59]. In their work on in vitro determination of layer-specific mechanical properties of human coronary arteries [59], Holzapfel and co-workers observed that the intima showed a significant **thickening**, a load-bearing capacity and a mechanical strength compared to the media and the adventitia. Moreover, the inclusion of the three layers in blood vessel modeling has a insignificant contribution on the shear stress [60]. **Furthermore, frontiers between the three layers are blurred in the arteriole [61]**. For aforementioned reasons, we chose to restrict arterial wall model to the intima. In this work, the thickness of **the arteriolar wall** is assigned to $20\mu\text{m}$ [57]. For reasons related to computational cost, we consider a section of a human arteriole ($L=300\mu\text{m}$). The arterial wall is assumed to be hyperelastic, homogenous and incompressible, the equation describing the motion is governed by

$$\rho_a \frac{\partial^2 \mathbf{u}^{(a)}}{\partial t^2} = \nabla \cdot \boldsymbol{\sigma}^{(a)} \quad (3)$$

where ρ_a is the arterial wall density, $\mathbf{u}^{(a)}$ the displacement vector and $\boldsymbol{\sigma}^{(a)}$ the Cauchy stress tensor. In addition, the constitutive relation can be written readily in terms of Cauchy stress tensor and strain-energy density function

$$\boldsymbol{\sigma}^{(a)} = J^{-1} \mathbf{F} \frac{\partial W^{(a)}}{\partial \mathbf{E}^{(a)}} \mathbf{F}^T$$

where J is the dilatation ratio, \mathbf{F} the deformation gradient tensor, $\mathbf{E}^{(a)}$ the Green-Lagrange strain tensor and $W^{(a)}$ the strain-energy density function which is related to the strain invariants by the following relation :

$$W^{(a)} = C_{10} (\bar{I}_1 - 3) + C_{01} (\bar{I}_2 - 3) + C_{20} (\bar{I}_1 - 3)^2 + C_{02} (\bar{I}_2 - 3)^2 + C_{11} (\bar{I}_1 - 3) (\bar{I}_2 - 3) + \frac{\kappa}{2} (J_{el} - 1)^2 \quad (4)$$

where $C_{10}, C_{01}, C_{20}, C_{02}$ and C_{11} denotes material parameters extracted by curve fitting from in vitro study [59] and adapted from [60] (see Table 1), \bar{I}_1 and \bar{I}_2 respectively denotes the first and the second invariant of the isochoric right Cauchy-Green deformation tensor, κ is the initial bulk modulus and J_{el} the elastic volume ratio. The Money-Rivlin constitutive law is based on the assumption of isotropic behavior throughout the deformation history. Note that the numerical values of C_{ij} parameters are provided from a study on human coronary arterial wall, in the lack of such study on human arteriole, we used the same values of C_{ij} . This extrapolation nevertheless remains acceptable since both vessels are of the same nature. **Regarding**

Table 1. Material parameters.

ρ (kg/m ³)	κ (Pa)	C_{10} (Pa)	C_{01} (Pa)	C_{20} (Pa)	C_{02} (Pa)	C_{11} (Pa)
1150	$2.04 \cdot 10^5$	$2.23 \cdot 10^5$	$1.37 \cdot 10^6$	$2.67 \cdot 10^6$	$3.71 \cdot 10^6$	$3.78 \cdot 10^6$

the external arteriolar wall, we consider a free unconstrained external wall (FEW) where the wall is free to deform and a constrained state where it is surrounded by a muscle which is more realistic. The muscle follows the Neo-Hookean law (5) [62]. Muscle thicknesses considered are $H_m = 5, 10, 15, 20, 27.5, 35$ and $60 \mu\text{m}$. The FEW assumption corresponds to $H_m = 0 \mu\text{m}$ (no surrounding muscle). As for the arteriolar wall, the zero displacement boundary condition is imposed to the ends of the muscle. Results relative to the FEW assumption and to the muscle-embedded arteriole are given on 4.2 and 4.4, respectively.

2.3 Microparticle model

The studied microparticle consists of a disk-shaped thin membrane (a thickness of $0.27\mu\text{m}$) enclosing an incompressible Newtonian fluid ($\eta_i = 0.00345\text{Pa} \cdot \text{s}$ and $\rho_i = 1000\text{kg/m}^3$). The membrane is treated as hyperelastic, isotropic and nearly incompressible surface in which the strain-energy density function for a Neo-Hookean material is given by :

$$W^{(m)} = \frac{G}{2} (\bar{I}_1 - 3) + \frac{\kappa}{2} (J_{el} - 1)^2 \quad (5)$$

where the parameter G (N/m^2) corresponds to the initial shear modulus. The initial bulk modulus κ and initial shear modulus G are calculated from the surface shear modulus G_s (N/m). In this framework the surface shear modulus is varied from the range of 10^{-2} to 10^{-3} N/m which is in the same range as experimental extracted modulus [28, 63]. A comprehensive and detailed review of constitutive relations can be found in [64].

In the membrane model, the stresses are integrated across the wall thickness and replaced by tensions, i.e., forces per unit length of the median deformed surface. The deformation of the microparticle is quantified by the Taylor parameter defined as:

$$D = \frac{|L_1 - L_2|}{L_1 + L_2} \quad (6)$$

where L_1 and L_2 respectively designate the axial and the radial length of the capsule (i.e. $D = 0$ for a disk-shaped microparticle). For the initial shape $L_1 = L_2 = 18 \mu\text{m}$. The Taylor parameter strongly depends on the nondimensional capillary number Ca . The latter measures the ratio between the viscous forces applied by the flow and elastic resistance of the membrane:

$$Ca = \frac{\eta \dot{\gamma} L_1}{2G_s} \quad (7)$$

2.4 Fluid-structure interaction

In this paragraph, the dynamic behavior of the suspended microparticle shall be obtained of the judicious interface conditions. Dynamic and kinematic **continuity** must be satisfied. Hence, the fluid-structure interaction pertaining the fluids is of non-homogeneous Dirichlet condition

$$\begin{aligned} \mathbf{v}^{(i)} &= \frac{\partial \mathbf{u}^{(m)}}{\partial t} \quad \text{at } (\Gamma_{fm}) \text{ (inside microparticle)} \\ \mathbf{v}^{(o)} &= \frac{\partial \mathbf{u}^{(m)}}{\partial t} \quad \text{at } (\Gamma_{fm}) \text{ (outside microparticle)} \\ \mathbf{v}^{(e)} &= \frac{\partial \mathbf{u}^{(a)}}{\partial t} \quad \text{at } (\Gamma_{fa}) \end{aligned}$$

representing mass conservation throughout the interface, and the fluid-structure interaction for the solids is of non-homogeneous Neumann

$$\begin{aligned} \boldsymbol{\sigma}^{(i)} \cdot \mathbf{n} &= \boldsymbol{\sigma}^{(m)} \cdot \mathbf{n} \quad \text{at } (\Gamma_{fm}) \text{ (inside microparticle)} \\ \boldsymbol{\sigma}^{(o)} \cdot \mathbf{n} &= \boldsymbol{\sigma}^{(m)} \cdot \mathbf{n} \quad \text{at } (\Gamma_{fm}) \text{ (outside microparticle)} \\ \boldsymbol{\sigma}^{(o)} \cdot \mathbf{n} &= \boldsymbol{\sigma}^{(a)} \cdot \mathbf{n} \quad \text{at } (\Gamma_{fa}) \end{aligned}$$

describing the equivalence of fluids stresses and solids stresses.

3 Numerical method

In the ALE description, the mesh is arbitrary connected to the coordinate system or to the material allowing large deformation state without a mesh distortion. In addition to material configuration R_X and spatial configuration R_x , a third referential configuration R_χ where reference coordinates χ identify the grid points is introduced. The computational grid is allowed to move independently on material motion with a given mesh velocity $\mathbf{v}_m = \partial \mathbf{x} / \partial t$ where \mathbf{x} is the physical coordinates of χ . The difference between both velocities refers to convective velocity $\mathbf{c} = \mathbf{v} - \mathbf{v}_m$ (Note that Eulerian description and Lagrangian description corresponds to $\mathbf{c} = \mathbf{v}$ and $\mathbf{c} = 0$, respectively). At fluid-structure interface, in addition to "classical" conditions given in 2.4, mesh velocity satisfies: $\mathbf{v}_m \cdot \mathbf{n} = \mathbf{v} \cdot \mathbf{n}$ where \mathbf{n} is the unit outward normal. In the moving referential mesh frame R_χ , the material time derivative of a scalar physical quantity f for a given particle X with respect to the moving mesh grid is described by the fundamental equation of ALE :

$$\frac{\partial f}{\partial t} \Big|_X = \frac{\partial f}{\partial t} \Big|_x + \frac{\partial f}{\partial x} \cdot \mathbf{c} \quad (8)$$

Regarding time-integration scheme, we used the implicit Backward Differentiation Formula (BDF) scheme (9) derived from the multistep Adams-Moulton scheme

$$\sum_{i=0}^k \alpha_i \mathbf{u}_{n-i} = \beta_0 h f(t_n, \mathbf{u}_n) \quad (9)$$

where h is the time-step, the order of accuracy k is varied from (10) :

$$\begin{aligned} k=1 : \alpha_0 = 1, \alpha_1 = -1, \beta_0 = 1 &\rightarrow \mathbf{u}_n = \mathbf{u}_{n-1} + h f(t_n, \mathbf{u}_n) \\ k=2 : \alpha_0 = 1, \alpha_1 = -\frac{4}{3}, \beta_0 = 1, \alpha_2 = \frac{1}{3} &\rightarrow \mathbf{u}_n = \frac{4}{3} \mathbf{u}_{n-1} - \frac{1}{3} \mathbf{u}_{n-2} + \frac{2}{3} h f(t_n, \mathbf{u}_n) \end{aligned} \quad (10)$$

The variables are updated at each time-step using a damped Newton nonlinear method [65]. This method is based on a damping reduction algorithm where the key parameter is the error E : For a new iteration $\mathbf{u}_1 = \mathbf{u}_0 + \lambda \delta u$ (where \mathbf{u}_0 is the initial guess, $10^{-5} \leq \lambda \leq 1$ the damping factor and δu the Newton time-step), the solver computes $Df(x)E = -f(\mathbf{u}_1)$ where $Df(x)$ is the Jacobian matrix and $f(\mathbf{u}_1)$ the residual vector of the solution vector \mathbf{u}_1 . If E is smaller than the relative error E_r , \mathbf{u}_1 is recomputed till the condition $E > E_r$ is satisfied. The nonlinear failures are dealt with the nonlinear controller (STAB) [66] that enables an efficient time-step control in the BDF method and ensures that the accuracy time-step h_{acc} remains smaller than the stability time-step h_{stab} . Mesh deformation is computed using Winslow smoothing nonlinear technique [67], the equations to solve are:

$$\frac{\partial^2 X}{\partial x^2} + \frac{\partial^2 X}{\partial y^2} = 0, \quad \frac{\partial^2 Y}{\partial x^2} + \frac{\partial^2 Y}{\partial y^2} = 0 \quad (11)$$

x and y are deformed mesh positions and, X and Y the reference coordinates of the material frame. An automatic remeshing procedure enables more extreme deformation states and prevents mesh reversing and tangling that lead to the deterioration of the results. The remeshing is automatically **activated** beyond a pre-determined cell quality threshold based on the criterion of equiangular skew: $\min \left[1 - \left[\max \left(\frac{\theta - \theta_e}{180 - \theta_e}, \frac{\theta_e - \theta}{\theta_e} \right) \right] \right] < 0.01$ where θ is the angle over a vertex in the element and θ_e the angle of the corresponding vertex in an ideal element (zero skewness). The discretization of fluid domain is done with P2/P1 element that gives a quadratic basis for velocity and linear pressure. This element satisfies the LBB (Ladyzhenskaya-Babuska-Brezzi) stability condition. Solving Navier-Stokes equations using finite element method is known to cause (as well as other convection driven problem) numerical instabilities. Therefore, a stabilization is required to circumvent numerical instabilities and solution oscillations. We use two methods of constant **stabilization**: streamline diffusion and crosswind diffusion. The first adds artificial diffusion in the streamline direction whereas the second adds diffusion in the cross direction. The added diffusion is a not physical but helps to avoid the mesh refinement and then a huge computational cost.

4 Results and discussion:

4.1 Validation of the numerical model

In this section, we report the validation of the present numerical model against the work of Barthes and co-workers on the dynamical **behavior** of a freely suspended spherical capsule in an unbounded shear flow [68]. In this work, the membrane of the microparticle is neo-Hookean. The external and internal fluids are similar, thus excluding buoyancy effect. The velocity and the pressure of both fluids are governed by Stokes equations ($Re \ll 1$). The FSI problem is solved by the ALE method. We performed a parametric calculation ($Ca = 0.075 - 0.6$) using the commercially available FEM package COMSOL Multiphysics. The evolution of Taylor parameter D is monitored till reaching an asymptotic deformation D^∞ (see Figure 2). Moreover, this evolution is similar to those reported in [37, 68], where the FSI problem is respectively solved using the boundary element method and the immersed boundary method. Note that the steady deformed shapes shown in Fig. 2 are identical to those illustrated in [68].

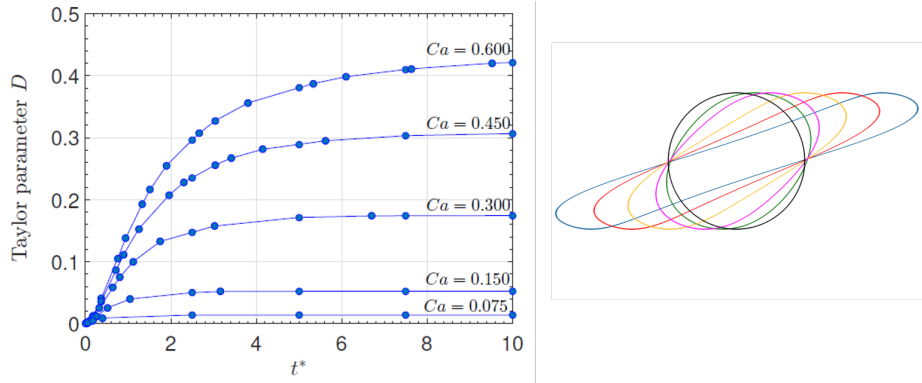


Fig. 2. Taylor parameter versus dimensionless time for a capsule suspended in a shear flow (left). Superposition of obtained steady deformed shapes illustrated by different colors: $Ca = 0.075$ (green) $Ca = 0.15$ (pink), $Ca = 0.3$ (yellow), $Ca = 0.45$ (red) and $Ca = 0.6$ (blue). Black color corresponds to the initial shape (right).

4.2 Microparticle confined in human arteriole

The dynamical response of the microparticle is investigated for $Ca = 0.01, 0.02, 0.03, 0.04$ and 0.05 . As shown in Figure 3(a), when the microparticle is flowing along the arteriole, the Taylor parameter becomes higher as the capillary number is increasing. In response to the sudden start of blood flow, microparticle becomes pebble-shaped: the initial rear end positive curvature (convexity) is decreased till a flattened state and the maximum radial length is significantly more important than the axial one ($t = 0.364$ ms in Figure 8(b)). As the microparticle moves from its initial position and starts flowing along the arteriole, it undergoes an axial extension while its radial dimension progressively decreases to compensate axial elongation. The obtained morphology referred to as bullet shape. In the immediate vicinity of the arteriole extremity ($t = 1.540$ ms), a concavity is observed at the rear of the microparticle (see Figure 8(b)).

The rear shape transition from the convexity to the flatness and then to the concavity and the increasing of front tapering (see Figure 8(b)) is a consequence of the wall displacement that changes the confinement and then the capillary number. As shown on Figure 4, at $t = 1$ ms, the rear end is convex for $Ca = 0.01$ while it is flattened for $Ca = 0.05$. Regarding the front, it is more pointed for $Ca = 0.05$. The decreasing of the initial rear convexity till the concavity and the increasing front tapering with increasing capillary number is observed in this work by varying "directly" the capillary number (via changing the membrane shear modulus) and "indirectly" (change induced by wall displacement). This behavior is reported in [22, 23] where the shape transition dependence on the capillary number is well described. For all Ca , the variations of

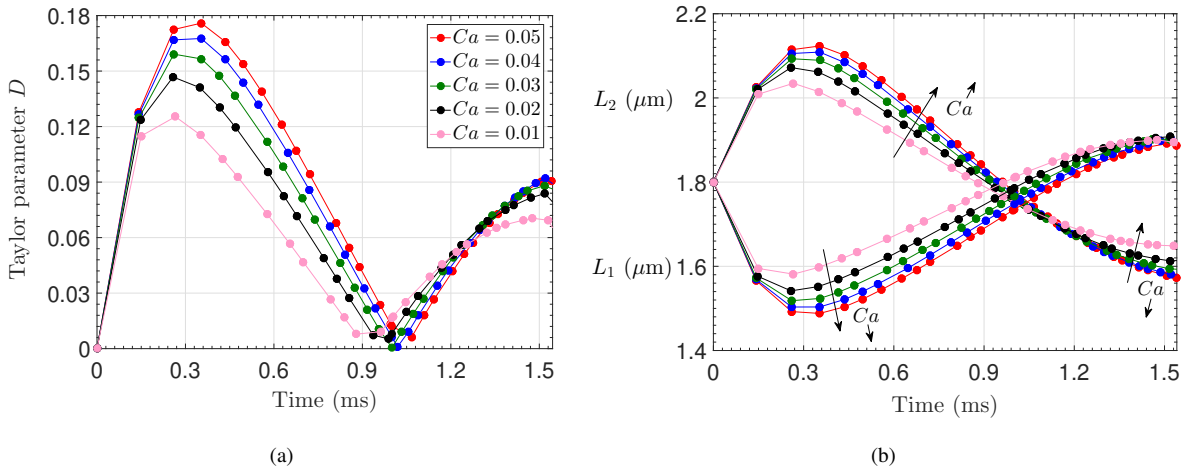


Fig. 3. Time-evolution of Taylor parameter (a) and of axial and radial lengths (b) for $Ca = 0.01 - 0.05$.

Taylor parameter versus time are parabolic with decreasing amplitudes. Indeed, the amplitude of the first lobe of the curve is nearly two time greater than the second one. For all curves, the ascending slope of the straight path is similar till roughly 0.15 ms. Above this point, curves deviate from their initial ascending straight path and different amplitudes are observed. Since the curves reached the maximum and starts to decrease, the minimum Taylor parameter is reached firstly for the less

important amplitude. Shortly thereafter, curves start to rise with the same slope from the lowest to the highest Ca , reason why in a certain zone, the trend is reversed and the deformation heightens from the lowest to the highest capillary number. Regarding the axial length L_1 and the radial length L_2 time-evolution (see Figure 3(b)), a symmetry with respect to the microparticle **centerline** is observed due to the surface-area conservation (a radial elongation is systematically compensated by an axial shrinking). The localized axial length change is the consequence of the edge effect. For the purpose of assessing

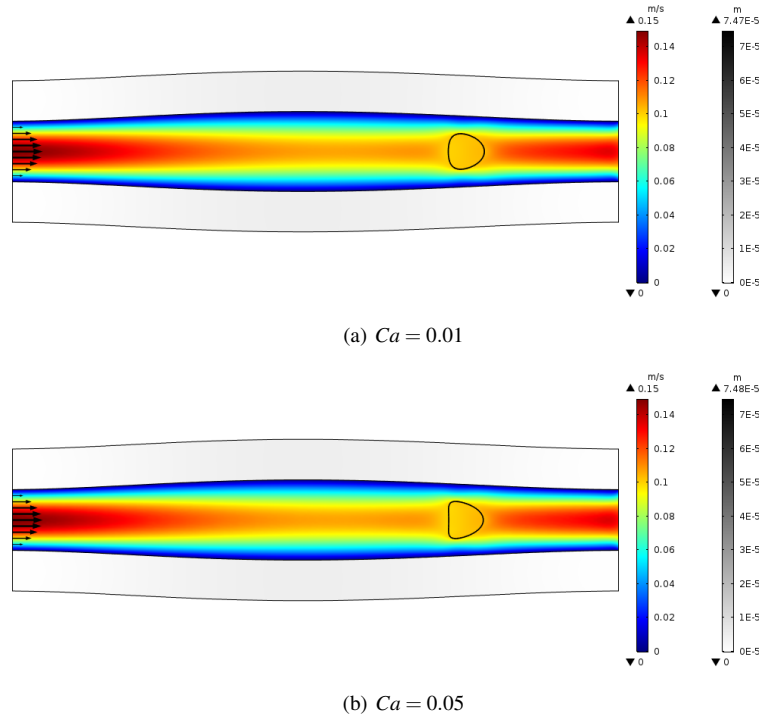


Fig. 4. Real time snapshot at $t = 1$ (ms). Rainbow color spectrum corresponds to velocity magnitude (m/s) and grey scale color to displacement (m).

the influence of shear-thinning of blood, we performed a comparison between the Newtonian blood model (so far used) and the Carreau model describing the shear-thinning. Obtained results for $Ca = 0.05$ have shown that deformation overtime is notably similar when the blood is considered as Newtonian or shear-thinning (see Figure 5). The slight discrepancies are due to the differences in the velocity profile and the wall shear stress. When the fluid is shear-thinning, the velocity profile is "flattened" and its slope near the wall is more important comparing to the Newtonian model, thus, the shear stress near the wall is more important. In order to display the parachute shape (a strongly concave rear end and a highly pointed front), the capillary number is increased until $Ca = 0.1$. Real time-snapshots: $t = 0.206, 1$ and 1.393 ms show respectively: pebble-shape (Figure 6(a)), bullet shape (Figure 6(b)) and parachute shape (Figure 6(c)). The observation reported above (the increasing concavity with respect to capillary number) is confirmed by the last calculation. Indeed, at $t = 1$ ms, we note the transition from the convex rear end ($Ca = 0.01$ in Figure 6(a)), to the flattened rear end ($Ca = 0.05$ in Figure 6(b)) and then to the concave rear end ($Ca = 0.10$ in Figure 6(c)). The increasing front sharpness is also confirmed. Local zoomed mesh illustrated in (Figure 6(d)) affirms the absence of mesh tangling /distortion. All of reported shapes for all capillary numbers are observed for artificial microparticles flowing in rectangular microchannel [22–25], RBCs [19–21] and a cancerous cell (except for the parachute shape) [69].

The effect of increasing arteriole length is evaluated for $L = 900$ and $1800 \mu\text{m}$. As for the initial length $L = 300 \mu\text{m}$, the time-evolution of Taylor parameter is concavity sign changing (Figure 7). One can remarks that for $L = 1800 \mu\text{m}$, the shape of the curve is identical to that of $L = 900 \mu\text{m}$ but "stretched". Even if the vascular resistance increases with length, we believe that the unsteadiness of Taylor parameter time-evolution will persists due to the mechanism of expansion-constriction that varies the viscous stresses acting on the microparticle (i.e. the capillary number).

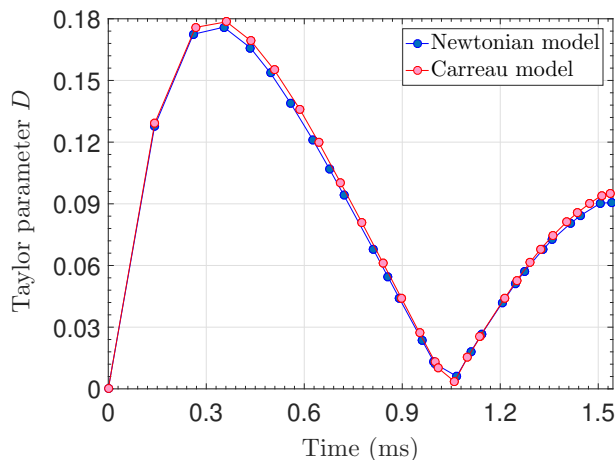


Fig. 5. Influence of the blood viscosity model for $Ca = 0.05$.

4.3 Comparison with rigid microchannel

A comparison with a rigid microchannel is performed for $Ca = 0.05$. It is concluded that for a similar capillary number, the **microparticle** exhibits a different dynamical behavior. Indeed, when the microparticle is confined in the rigid channel, the Taylor parameter evolution with respect to time is ascending till the microparticle is stopped by the channel extremity (see Figure 8(a)). This evolution is akin when the microparticle is subjected to a shear flow [27, 68] or to an elongational flow [63]. Nevertheless, the horizontal plateau is not observed because of the edge effect. Moreover, various deformed shapes are observed for the hyperelastic arterial wall while the particle confined in the rigid channel is deformed into a quasi-steady shape (see Figures 8(b) and 8(c)). Time-snapshots show that at similar times ($t = 0.364, 0.698$ and 0.910 ms), deformed shapes are widely different. The deformation soars in the case of arterial wall whilst it progressively increases with respect to time (see Figure 8(a)). On the other hand, when the particle flows along the rigid microchannel, it attains the channel extremity at $t = 0.910$ ms, while at the same time, the microparticle suspended in the arteriole is in the midway (see Figure 8(b)) which reveals that the microparticle moves with different velocities. According to the microparticle rear end velocity time-evolution, the flowing particle in the rigid microchannel attains a maximum velocity before it decelerates quasi-instantly and tends to an asymptotic velocity (see Figure 9). Furthermore, the microparticle confined in arteriole accelerates along its course. Curves show that for the highest and the lowest capillary number ($Ca = 0.01, Ca = 0.05$), a slight gap exists till a certain time ($t \approx 0.3$ ms) and the curves finally coincide. This result suggests that for any capillary number, velocity tends to a common magnitude. All of observed discrepancies are due to the arterial wall distensibility and its hyperelastic response to the flow. The expansion-constriction changes the confinement and therefore the shear rate (i.e. viscous forces applied on the flowing particle). In these conditions, viscous forces applied on the microparticle are related to the wall displacement, leading to different deformed shapes for a same capillary number. In contrast, in the case of rigid microchannel, the microparticle is deformed into a quasi-steady shape. For a deformable wall, it is more appropriate to talk about an initial capillary number that correspond to the undeformed wall state.

4.4 Arteriole embedded in muscle

In this paragraph, we report the effect of the presence of a surrounding muscle on arteriolar wall displacement and on deformation of the microparticle. This configuration is more realistic than the FEW assumption. As expected, it is found that the presence of the muscle that serves as a uniform mechanical load, restricts both arteriolar wall vertical displacement (Figure 10) [70] and microparticle deformation (Figure 11). The higher the muscle thickness the less the arteriolar wall dilation upon blood flow. In the absence of the surrounding muscle, the maximum dilation of the arteriole (34.02%) is within the range of experimental dilation values reported for human coronary arteriole in [71]. The maximum of Taylor parameter is constant starting from $H_m = 35 \mu\text{m}$ (Figure 11). A comparison performed for $H_m = 60 \mu\text{m}$ and the rigid wall reveals that both configurations are quasi-identical (discrepancies are comprised between 0.89% and 4.31%).

5 Implications of results in a medical context

Whether in the presence of the surrounding muscle ($H_m < 35 \mu\text{m}$) or in its absence, it is found that microparticle deformation is increased comparing to the rigid wall assumption. In a context of medical application, an important deformation is potentially a risk of premature burst in the vicinity of a non-targeted environment which implies toxic effects on healthy

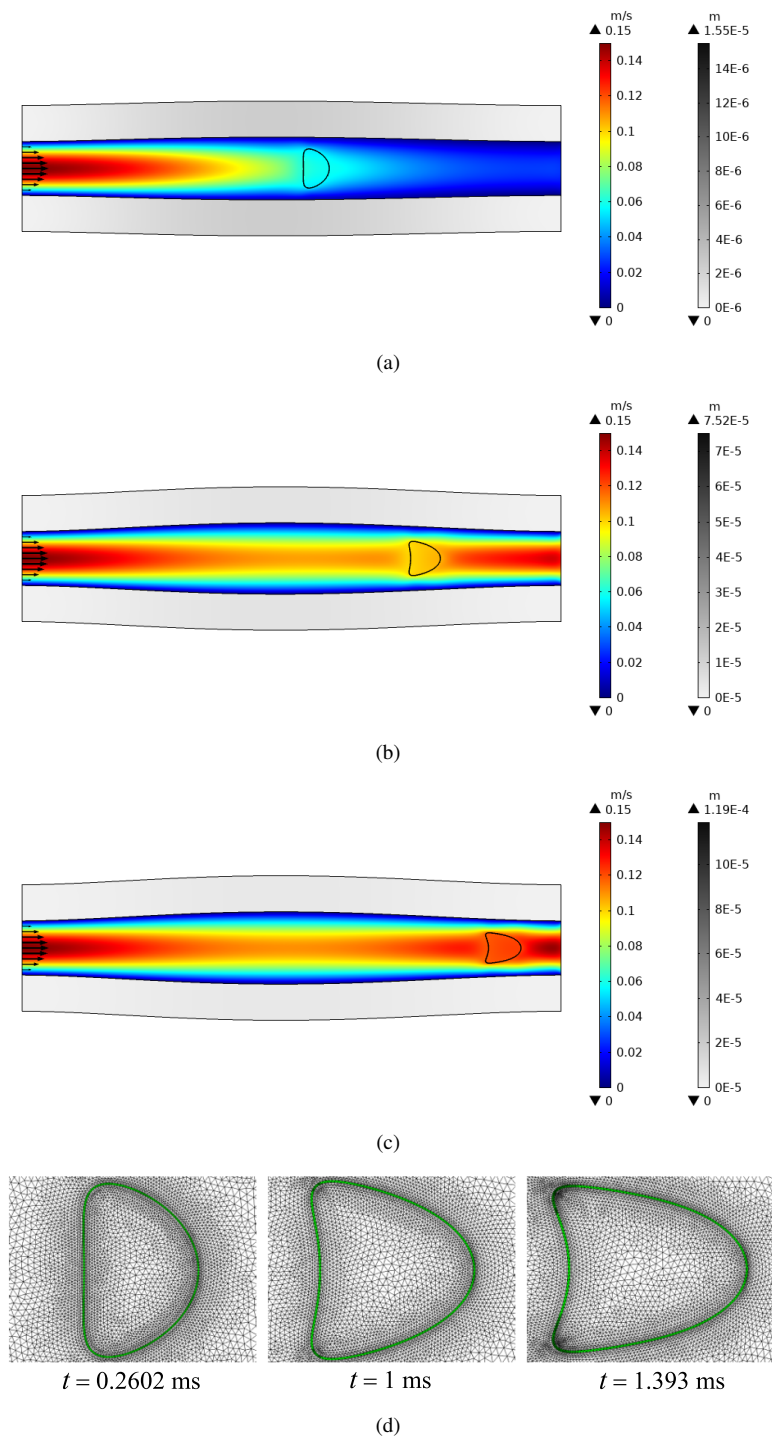


Fig. 6. Pebble-shaped microparticle at $t = 0.2602$ ms (a). Bullet-shaped microparticle at $t = 1$ ms (b). Parachute-shaped microparticle with a strongly concave rear end at $t = 1.393$ ms (c) Corresponding local mesh zoom (d).

tissues. Regarding the velocity, the arteriolar wall distensibility is found to decelerates the microparticle. Firstly, that means that the particle is in longer contact with RBCs and white blood cells and knowing that these biological cells (which size is comparable to the studied microparticle) imposes stresses on microparticle membrane and consequently, a longer contact could result in an additional burst risk. Secondly, the microparticle could impedes bloodstream flow. These findings must imperatively be taken into account while designing microparticles in order to ensure a safe and efficient functioning of the drug-eluting microparticles.

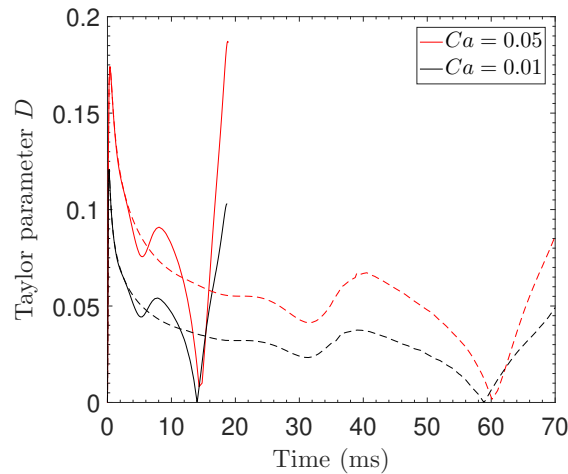


Fig. 7. Arteriole length effect on Taylor parameter. Solid lines are for $L = 900\mu\text{m}$ and dashed lines for $L = 1800\mu\text{m}$.

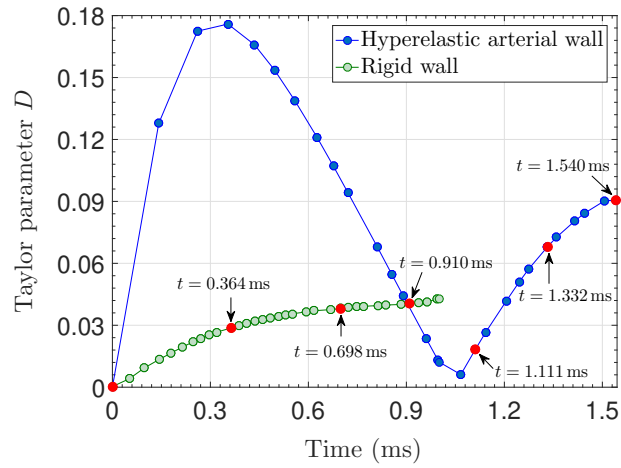
Conclusions

In this research paper, we investigate the dynamical behavior of a soft microparticle confined by hyperelastic arterial wall and suspended in blood flow, while fully respecting biomechanical constraints. Finding reveals that the wall distensibility has a great influence on microparticle deformation (qualitatively and quantitatively) and on its flowing velocity along the arteriole. We unambiguously outline the relevance of the inclusion of biomechanical constraints **for an accurate prediction of microparticle dynamics, a prerequisite of a safe and proficient targeted drug-delivery procedure**. This study is the first of its kind and further investigation remains necessary, in particular a realistic vessel geometry instead of the idealized geometry used for the sake of simplicity. The following concluding remarks could be drawn :

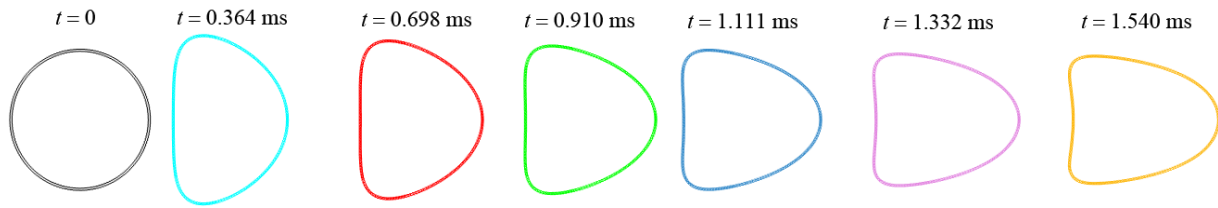
- The deformation and the velocity of the microparticle depend on mechanical properties of the wall.
- The displacement of the wall changes the shear rate and then the viscous forces applied on the microparticle membrane.
- The microparticle rear end and front shape transition and their dependence on the capillary number are in good agreement with the numerical and experimental observations reported in numerous published studies.
- Deformed shapes are morphologically in excellent agreement with literature.

References

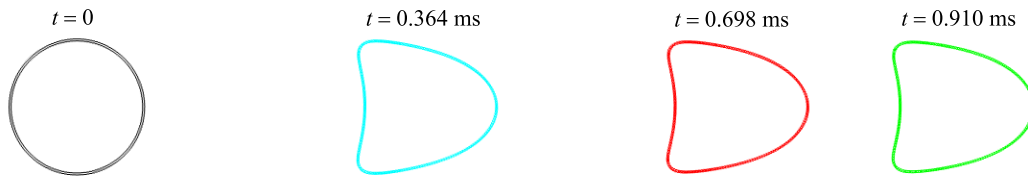
- [1] O. V. Chumakova, A. V. Liopo, V. G. Andreev, I. Cicenaitis, B. M. Evers, S. Chakrabarty, T. C. Pappas and R. O. Esenaliev. Composition of PLGA and PEI/DNA nanoparticles improves ultrasound-mediated gene delivery in solid tumors in vivo, *Cancer Lett.* **261**(2), 215–225 (2008).
- [2] J. Shao, M. Xuan, T. Si, L. Dai and Q. He. Biointerfacing polymeric microcapsules for in vivo near infrared light-triggered drug release, *Nanoscale.* **7**(45), 19092–19098 (2015).
- [3] J. Ma, L. Du, M. Chen, H. Wang, L. Xing, L. Jing and Y. Li. Drug-loaded nano-microcapsules delivery system mediated by ultrasound-targeted microbubble destruction: A promising therapy method, *Biomed. Reports,* **1**(4), 506–510 (2013).
- [4] P. Soon-Shiong. Treatment of type I diabetes using encapsulated islet. *Adv. Drug Deliv. Rev.* **35**(2-3), 259–270 (1999).
- [5] E. Mihalko, K. Huang, E. Sproul, K. Cheng and A. C. Brown. Targeted treatment of ischemic and fibrotic complications of myocardial infarction using a dual-delivery microgel therapeutic, *ACS Nano.* **12**(8), 7826–7837 (2018).
- [6] M. R. Dreher, K. V. Sharma, D. L. Woods, G. Reddy, Y. Tang, W. F. Pritchard, O. A. Chiesa, J. W. Karanian, J. A. Esparza, D. Donahue, E. B. Levy, S. L. Willis, A. L. Lewis and B. J. Wood. Radiopaque Drug-Eluting Beads for Transcatheter Embolotherapy: Experimental study of Drug Penetration and Coverage in Swine, *Journal of Vascular and Interventional Radiology* **23**(2), 257–264(2012).
- [7] A. Hagan, M. Caine, C. Press, W. M. Macfarlane, G. Phillips, A. W. Lloyd, P. Czuczman, H. Kilpatrick, Z. Bascalb, Y. Tang, P. Garcia and A. L. Lewis. Predicting pharmacokinetic behaviour of drug release from drug-eluting embolization beads using in vitro elution methods, *European Journal of Pharmaceutical Sciences* **136**, 104943 (2019).
- [8] T. de Baere, S. Plotkin, R. Yu, A. Sutter, Y. Wu and G. M. Cruise. An In Vitro Evaluation of Four Types of Drug-Eluting Microspheres Loaded with Doxorubicin, *Journal of Computational Physics* **27**, 1425–1431(2016).
- [9] K. Fuchs, P. E. Bize, O. Dormond, A. Denys, E. Doelker, G. Borchard and O. Jordan. Drug-eluting beads loaded with antiangiogenic agents for chemoembolization: in vitro sunitinib loading and release and in vivo pharmacokinetics in an animal model, *Journal of Vascular and Interventional Radiology* **25**(3), 379–387 (2014).



(a)



(b)



(c)

Fig. 8. Taylor parameter and microparticle deformed shapes for $Ca = 0.05$. (a) Red markers at specific times point out snapshot time used to capture deformed shapes. (b) Real time snapshots of the microparticle flowing along the hyperelastic arteriole (b) and along the rigid microchannel (rigid wall) (c).

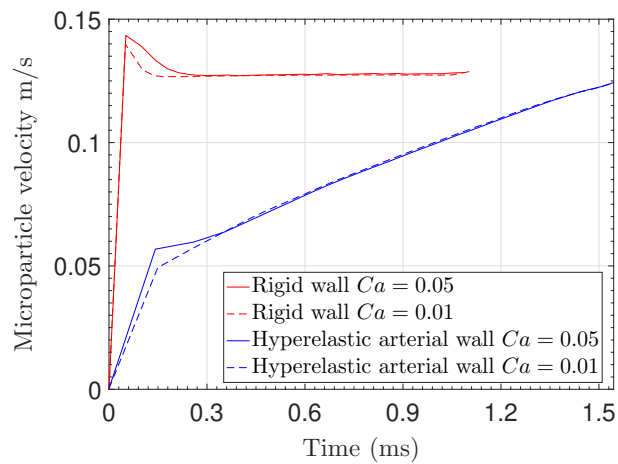


Fig. 9. Microparticle rear velocity for $Ca = 0.01$ and $Ca = 0.05$.

[10] R. R. Taylor, Y. Tang, M. V. Gonzalez, P. W. Stratford and A. L. Lewis. Irinotecan drug eluting beads for use in chemoembolization: In vitro and in vivo evaluation of drug release properties, *European Journal of Pharmaceutical*

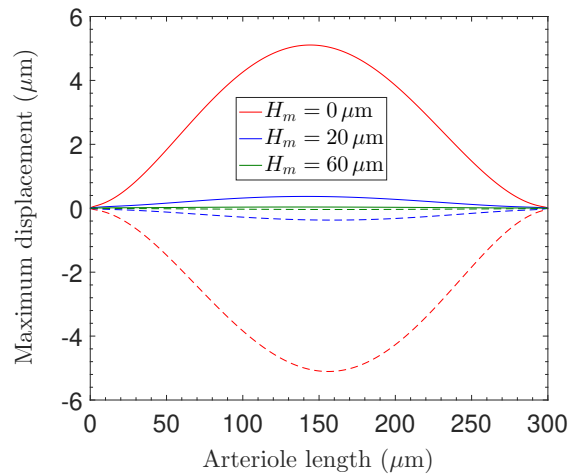


Fig. 10. Maximum arteriolar wall dilation with respect to arteriole length. Solid lines are for upper wall displacements and dashed lines for lower wall displacements.

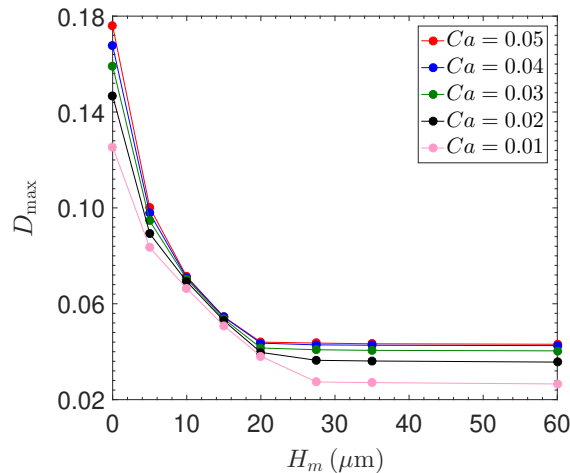


Fig. 11. Effect of varying muscle thickness on maximum Taylor parameter D_{max} .

Sciences **30**, 7–14 (2007).

- [11] J. M. Sosa, N. D. Nielsen, S. M. Vignes, T. G. Chen and S. S. Shevkoplyas. The relationship between red blood cell deformability metrics and perfusion of an artificial microvascular network, *Clin. Hemorheol. Microcirc.* **57**(3), 291–305 (2014).
- [12] J. M. Burns, X. Yang, O. Forouzan, J. M. Sosa and S. S. Shevkoplyas. Artificial microvascular network: A new tool for measuring rheologic properties of stored red blood cells, *Transfusion*, **52**(5), 1010–1023 (2012).
- [13] S. Hé, G. Lenormand, A. Richert and F. Ois Gallet. A new determination of the shear modulus of the human erythrocyte membrane using optical tweezers, *Biophysical. Journal.* **76**, 1145–1151 (1999).
- [14] R. Hochmuth. Erythrocyte Membrane Elasticity And Viscosity. *Annu. Rev. Physiol.* **49**(1), 209–219 (1987).
- [15] R. Waugh and E. A. Evans. Thermoelasticity of red blood cell membrane, *Biophys. Journal.* **26**(1), 115–131 (1979).
- [16] E. A. Evans, R. Waugh and L. Melnik. Elastic area compressibility modulus of red cell membrane, *Biophys. Journal.* **6**, 585–595 (1976).
- [17] M. A. Peterson, H. Strey and E. Sackmann. Theoretical and phase contrast microscopic eigenmode analysis of erythrocyte flicker: amplitudes, *J. Phys. II*, **2**(5), 1273–1285 (1992).
- [18] E. Sackmann. The Seventh Datta Lecture Membrane bending energy concept of vesicle-and cell-shapes and shape-transitions, *FEBS Letters.* **346**(1), 3–16 (1994).
- [19] H. Noguchi and G. Gompper. Shape transitions of fluid vesicles and red blood cells in capillary flows, *Proc. Natl. Acad. Sci.* **102**(40), 14159–14164 (2005).
- [20] G. Tomaiuolo, L. Lanotte, R. D’Apolito, A. Cassinese and S. Guido. Microconfined flow behavior of red blood cells,

- Med. Eng. Phys.* **38**(1), 11–16 (2016).
- [21] B. Kaoui, G. Birois and C. Misbah. Why do red blood cells have asymmetric shapes even in a symmetric flow? *Phys. Rev. Lett.* **103**(18) (2009).
- [22] G. Coupier, A. Farutin, C. Minetti, T. Podgorski and C. Misbah. Shape diagram of vesicles in poiseuille flow, *Phys. Rev. Lett.* **108**(17) (2012).
- [23] S. Kuriakose and P. Dimitrakopoulos. Deformation of an elastic capsule in a rectangular microfluidic channel, *Soft Matter* **9**(16), 4284–4296 (2013).
- [24] X. Q. Hu, B. Sévénie, A. V. Salsac, E. Leclerc and D. Barthès-Biesel. Characterizing the membrane properties of capsules flowing in a square-section microfluidic channel: Effects of the membrane constitutive law, *Phys. Rev. E - Stat. Nonlinear, Soft Matter Phys.* **87**(6), (2013).
- [25] J. Gubspun, C. de Loubens, R. Trozzo, J. Deschamps, M. Georgelin, F. Edwards-Levy and J. M. Leonetti. Perturbations of the flow induced by a microcapsule in a capillary tube, *Fluid Dyn. Res.* **49**(3) (2017).
- [26] M. Rachik, D. Barthès-Biesel, M. Carin and F. Edwards-Levy. Identification of the elastic properties of an artificial capsule membrane with the compression test: Effect of thickness, *J. Colloid Interface Sci.* **301**(1), 217–226 (2006).
- [27] M. Husmann, H. Rehage, E. Dhenin and D. Barthès-Biesel. Deformation and bursting of nonspherical polysiloxane microcapsules in a spinning-drop apparatus, *J. Colloid Interface Sci.* **282**, 109–119 (2005).
- [28] Y. Lefebvre, E. Leclerc, D. Barthès-Biesel, J. Walter and F. Edwards-Lévy. Flow of artificial microcapsules in microfluidic channels: A method for determining the elastic properties of the membrane, *Phys. Fluids*, **20**(12) (2008).
- [29] R. M. Kleinberger, N. A. D. Burke, K. Dalnoki-Veress and H. D. H. Stover. Systematic study of alginate-based microcapsules by micropipette aspiration and confocal fluorescence microscopy, *Mater. Sci. Eng. C* **33**(7), 4295–4304 (2013).
- [30] M. Carin, D. Barthès-Biesel, F. Edwards-Lévy, C. Postel and D. C. Andrei. Compression of biocompatible liquid-filled HSA-alginate capsules: Determination of the membrane mechanical properties, *Biotechnol. Bioeng.* **82**(2), 207–212 (2003).
- [31] Z. Wang, Y. Sui, A. V. Salsac, D. Barthès-Biesel and W. Wang. Motion of a spherical capsule in branched tube flow with finite inertia, *J. Fluid Mech.* **806**, 603–626 (2016).
- [32] Y. Lefebvre and D. Barthès-Biesel. Motion of a capsule in a cylindrical tube: Effect of membrane pre-stress, *J. Fluid Mech.* **589**, 157–181 (2007).
- [33] D. Barthès-Biesel, A. Diaz and E. Dhenin, Effect of constitutive laws for two-dimensional membranes on flow-induced capsule deformation, *J. Fluid Mech.* **460**, 211–222 (2002).
- [34] A. Leyrat-Maurin and D. Barthès-Biesel. Motion of a Deformable Capsule Through a Hyperbolic Constriction, *J. Fluid Mech.* **279**, 135–163 (1994).
- [35] Z. X. Gong and C. J. Lu. Research on the spherical capsule motion in 3D simple shear flows, *J. Shanghai Jiaotong Univ.* **15**(6), 702–706, (2010).
- [36] X. Q. Hu, A. V. Salsac and D. Barthès-Biesel. Flow of a spherical capsule in a pore with circular or square cross-section, *J. Fluid Mech.* **705**, 176–194 (2012).
- [37] P. Pranay, S. G. Anekal, J. P. Hernandez-Ortiz and M. D. Graham. Pair collisions of fluid-filled elastic capsules in shear flow: Effects of membrane properties and polymer additives, *Phys. Fluids* **22** (2010).
- [38] D. Barthès-Biesel and J. M. Rallison. The time-dependent deformation of a capsule freely suspended in a linear shear flow, *J. Fluid Mech.* **113**, 251–267 (1981).
- [39] R. Skalak, A. Tozeren, R. P. Zarda and S. Chien. Strain Energy Function of Red Blood Cell Membranes, *Biophys. J.* **13**(3), 245–264 (1973).
- [40] E. A. Evans and R. Skalak. *Mechanics and thermodynamics of biomembranes* **35**, CRC Press (1980).
- [41] O. H. Yeoh. Some Forms of the Strain Energy Function for Rubber, *RUBBER Chem. Technol.* **66**(5), 754–771 (1993).
- [42] A. Diaz, N. Pelekasis and D. Barthès-Biesel. Transient response of a capsule subjected to varying flow conditions: Effect of internal fluid viscosity and membrane elasticity, *Phys. Fluids* **12**(5), 948–957 (2000).
- [43] C. Dupont, P. Le Tallec, D. Barthès-Biesel, M. Vidrascu and A. V. Salsac. Dynamics of a spherical capsule in a planar hyperbolic flow: Influence of bending resistance, *Procedia IUTAM* **16**, 70–79 (2015).
- [44] S. Kwak and C. Pozrikidis. Effect of membrane bending stiffness on the axisymmetric deformation of capsules in uniaxial extensional flow, *Phys. Fluids* **13**(5), 1234–1242 (2001).
- [45] C. Pozrikidis. Effect of membrane bending stiffness on the deformation of capsules in simple shear flow, *J. Fluid Mech.* **440**, 269–291 (2001).
- [46] N. Tahiri. Simulation de Globules Rouges modèles, et analyse analytique de modèles de suspensions très concentrées, Université de Grenoble et Université Mohammed V Rabat (2010).
- [47] Comsol Multiphysics, Analysis User's Manual Version 5.2 (2016).
- [48] D. E. Brooks, J. W. Goodwin and G. V Seaman. Interactions among erythrocytes under shear, *J. Appl. Physiol.* **28**(2), 172–177 (1970).
- [49] S. Chien. Shear dependence of effective cell volume as a determinant of blood viscosity, *Science* **168**(3934), 977–979

(1970).

- [50] S. A. Berger and L. D. Jou. Flows in Stenotic Vessels, *Annu. Rev. Fluid Mech.* **32**(1), 347–382, (2002).
- [51] A. M. Robertson, A. Sequeira and M. V. Kameneva. *Hemodynamical flows Oberwolfach Seminars*, 37th ed. Birkhauser Verlag (2008).
- [52] G. Koutsiaris, S. V. Tachmitzi and N. Batis. Wall shear stress quantification in the human conjunctival pre-capillary arterioles in vivo, *Microvasc. Res.* **85**(1), 34–39 (2013).
- [53] I. C. Young and R. Kenneth. Effects of the non-Newtonian viscosity of blood on flows in a diseased arterial vessel. Part 1: steady flows, *Biorheology* **28**(199), 241–262 (1991).
- [54] J. R. Womersley. Method for the calculation of velocity, rate of flow and viscous drag in arteries when the pressure gradient is known, *J. Physiol* **127**, 553–563 (1955).
- [55] C. G. Caro, T. J. Pedley, R. C. Schroter, W. A. Seed. *The Mechanics of the circulation*, **35**(1st ed. Oxford University Press, 1978).
- [56] D. N. Ku. Blood flow in arteries, *Annu. Rev. Fluid Mech.* **29**(1), 399–434 (1997).
- [57] K. E. Barrett, S. M. Barman, S. Boitano and H. Brooks. *Ganong's Review of Medical Physiology*, 23th ed. McGraw Hill Medical (2012).
- [58] A. Taki, A. Kermani, S. M. Ranjbarnavazi and A. Pourmodheji, Chapter 4 - Overview of Different Medical Imaging Techniques for the Identification of Coronary Atherosclerotic Plaques, *Computing and Visualization for Intravascular Imaging and Computer-Assisted Stenting* 1st ed. Academic Press (2017).
- [59] G. A. Holzapfel, G. Sommer, C. T. Gasser and P. Regitnig. Determination of layer-specific mechanical properties of human coronary arteries with nonatherosclerotic intimal thickening and related constitutive modeling, *Am. J. Physiol. Circ. Physiol.* **289**(5), 2048–2058 (2005).
- [60] A. Gholipour, M. H. Ghayesh, A. Zander and R. Mahajan. Three-dimensional biomechanics of coronary arteries, *Int. J. Eng. Sci.* **130**(130), 93–114 (2018).
- [61] L. A. Martinez-Lemus. The Dynamic Structure of Arterioles, *Basic Clinical Pharmacology Toxicology* **110**, 5–11(2012).
- [62] T. A. Cheema and C. W. Park. Numerical investigation of hyperelastic wall deformation characteristics in a micro-scale stenotic blood vessel, *Korea-Australia Rheology* **25**, 121–127(2013).
- [63] C. De Loubens, J. Deschamps, M. Georgelin, A. Charrier, F. Edwards-Levy and M. Leonetti. Mechanical characterization of cross-linked serum albumin microcapsules, *Soft Matter* **10**(25), 4561–4568 (2014).
- [64] L. A. Taber. *Nonlinear Theory of Elasticity: Applications in Biomechanics*, World Scientific Publishing Co Pte Ltd (2004).
- [65] P. Deuffhard. A modified Newton method for the solution of ill-conditioned systems of nonlinear equations with application to multiple shooting, *Numerische Mathematik* **22**, 289–315(1974).
- [66] P. K. Moore and L. R. Petzold. A Stepsize Control Strategy for Stiff Systems of Ordinary Differential Equations, *Alied Numerical Mathematics* **15**, 449–463 (1994).
- [67] A. M. Winslow. Numerical solution of the quasilinear poisson equation in a nonuniform triangle mesh *Journal of Computational Physics* **2** **1**(2), 149–172 (1967).
- [68] E. Lac, D. Barthès-Biesel, N. A. Pelekasis and J. Tsamopoulos. Spherical capsules in three-dimensional unbounded Stokes flows: Effect of the membrane constitutive law and onset of buckling, *J. Fluid Mech.* **35**(516), 303–334 (2004).
- [69] M. Dabagh, A. Randles. Role of deformable cancer cells on wall shear stress- associated-VEGF secretion by endothelium in microvasculature, *PLoS ONE*. **14** (2), (2019).
- [70] N. Westerhof, C. Boer, R. R. Lamberts and P. Sipkema. Cross-Talk Between Cardiac Muscle and Coronary Vasculature, *Physiological Reviews* **86**, 1263–1308(2006).
- [71] H. Miura, R. E. Wachtel, Y. Liu, F. R. Loberiza, T. Saito, M. Miura and D. D. Gutterman. Flow-Induced Dilatation of Human Coronary Arterioles Important Role of Ca^{2+} Activated K^{+} Channels, *Circulation* **103**, 1992–1998 (2001).